Electronic Supplementary Material (ESI) for Nanoscale.
This journal is © The Royal Society of Chemistry 2020

Supplementary Information

Volume and concentration dosing in pico-litres using two-channel microfluidic AFM cantilever

E.J. Verlinden, M. Madadelahi, E. Sarajlic, A. Shamloo, A.H. Engel, U. Staufer and M. K.Ghatkesar

March 31, 2020

Movies description

• Movie 1: Simulation - concentration single-phase.
In this simulation, the concentration contour (mol/m^3) of the fluorescein is shown in different times. The simulation follows the procedure of Table S2-case3. In first 5 seconds (from t=0s to 5s) the fluorescein is dispensing into the surrounding water and in the second 5 seconds (from t=5s to 10s) the outside fluid is aspirating into the cantilever.

• Movie 2: Simulation - volume fraction two-phase
In this simulation, the volume fraction of air (grey) and fluorescein (white) are shown in different times. This simulation shows the meniscus between gas/liquid phases which is moving by time.

• Movie 3: Fluorescein meniscus in a aperture-clogged cantilever.
Moving a fluorescein meniscus by applying $\Delta P_{Leg1} = 0\,\text{mbar}$ and $\Delta P_{Leg2} = 200\,\text{mbar}$, the fluid goes back as soon as the pressure is released. The cantilever is in air as an outside medium. The tip aperture was clogged in this experiment.

• Movie 4: Dosing Fluorescein in air environment.
This movie shows that fluorescein was dispensed onto the cantilever top surface in air medium while applying $\Delta P_{Leg1} = 2\,\text{bar}$. The fluorescent signal originates from fluorescein coming out through the apertures and forming a large droplet on the outside surface of the cantilever.

• Movie 5: Dosing rhodamine in air environment.
After dispensing fluorescein, by shifting the overpressure application to leg 2, $\Delta P_{Leg2} = 2.1\,\text{bar}$, rhodamine-labelled liposome solution could be dispensed. A growing droplet on top of the cantilever was visualized. Individual rhodamine particles are seen flowing through the legs of the cantilever.

• Movie 6: Dosing fluorescein in water.
Dspensing at $\Delta P_{Leg1} = 500\,\text{mbar}$ and $\Delta P_{Leg2} = 0\,\text{mbar}$ for 5 s, fluorescein was dispensed into outside water medium.

• Movie 7: Aspirating water from surrounding medium.
First dispensing fluorescein for 5 s at $\Delta P_{Leg1} = 500\,\text{mbar}$ and $\Delta P_{Leg2} = 0\,\text{mbar}$, then aspirating water into leg 2 at $\Delta P_{Leg1} = 0\,\text{mbar}$ and $\Delta P_{Leg2} = -50\,\text{mbar}$ for 20 s.

• Movie 8: Co-dosing fluorescein and water in water.
First dispensing fluorescein for 5 s at $\Delta P_{Leg1} = 500\,\text{mbar}$ and $\Delta P_{Leg2} = 0\,\text{mbar}$, then aspirating water at $\Delta P_{Leg1} = 0\,\text{mbar}$ and $\Delta P_{Leg2} = -50\,\text{mbar}$ for 5 s into leg 2, then dispensing water and fluorescein at $\Delta P_{Leg1} = 80\,\text{mbar}$ and $\Delta P_{Leg2} = 200\,\text{mbar}$ for 5 s.

1 Atomic Force Microscopy

The two channel microfluidic AFM cantilever has been used to image a pattern in the tapping mode. This is to prove that the tip despite being hollow can still be used for regular AFM imaging.

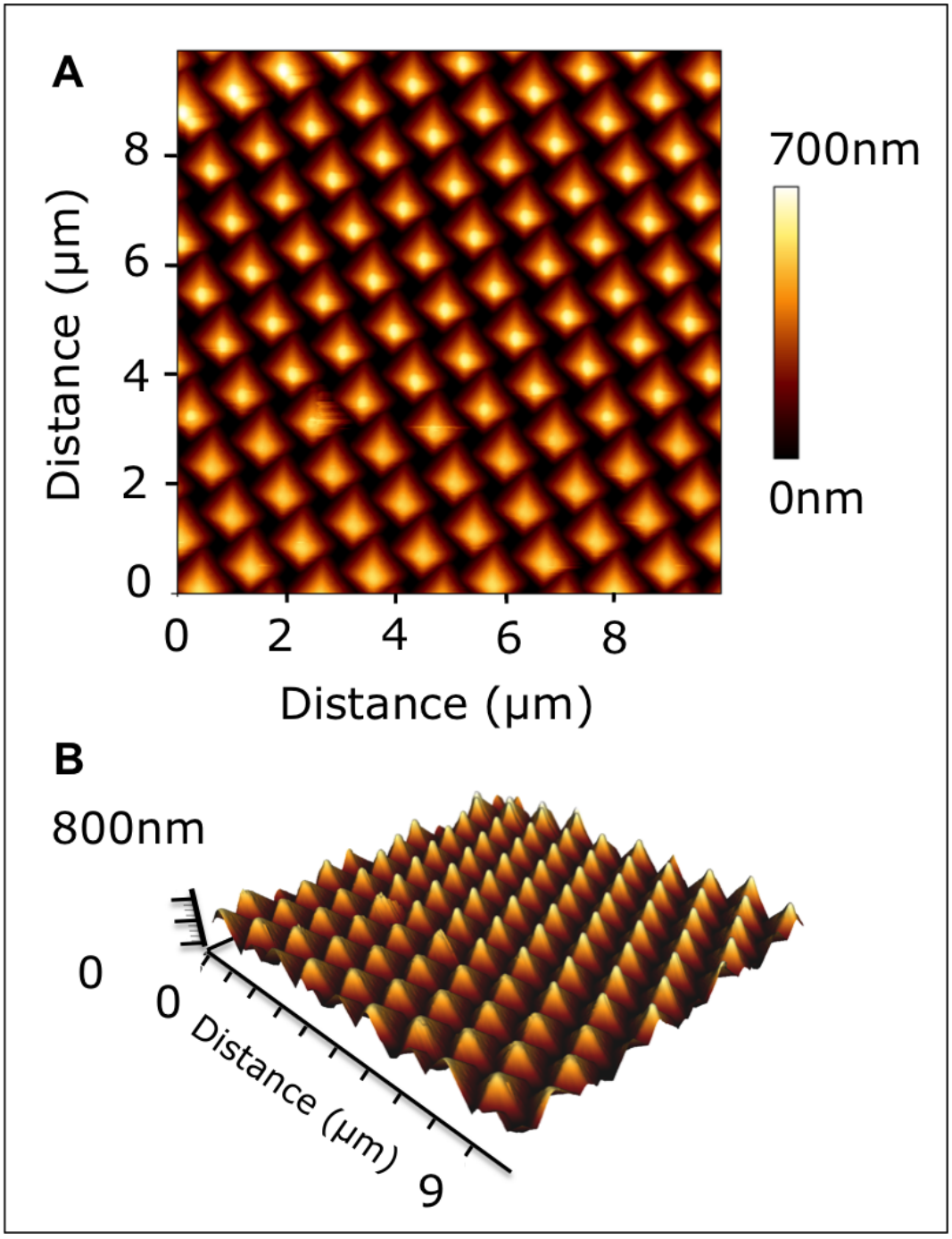

Figure S1: The two-channel microfluidic AFM cantilever probe was operated in the tapping mode to image a nano-pillar array of diameter 200 nm and 1000 nm height. A) Top view and B) 3D view of the pillar array. The pyramidal tip artefact can be see in the pillar shapes obtained, cylindrical pillars look pyramidal. These images prove the AFM functionality of the probe.

2 Numerical model validation

The device geometry at the tip is quite complicated. There is a small pyramid inside (not visible from outside) the big external (visible from outside) pyramid. Just before the big pyramid, the fluidic channels are physically split into two channels resulting in a total of four channels. These four channels merge inside a small pyramid, where fluids mix before exiting through the apertures. Two apertures were made on the small pyramid (Figure S2). See also main article for device details.

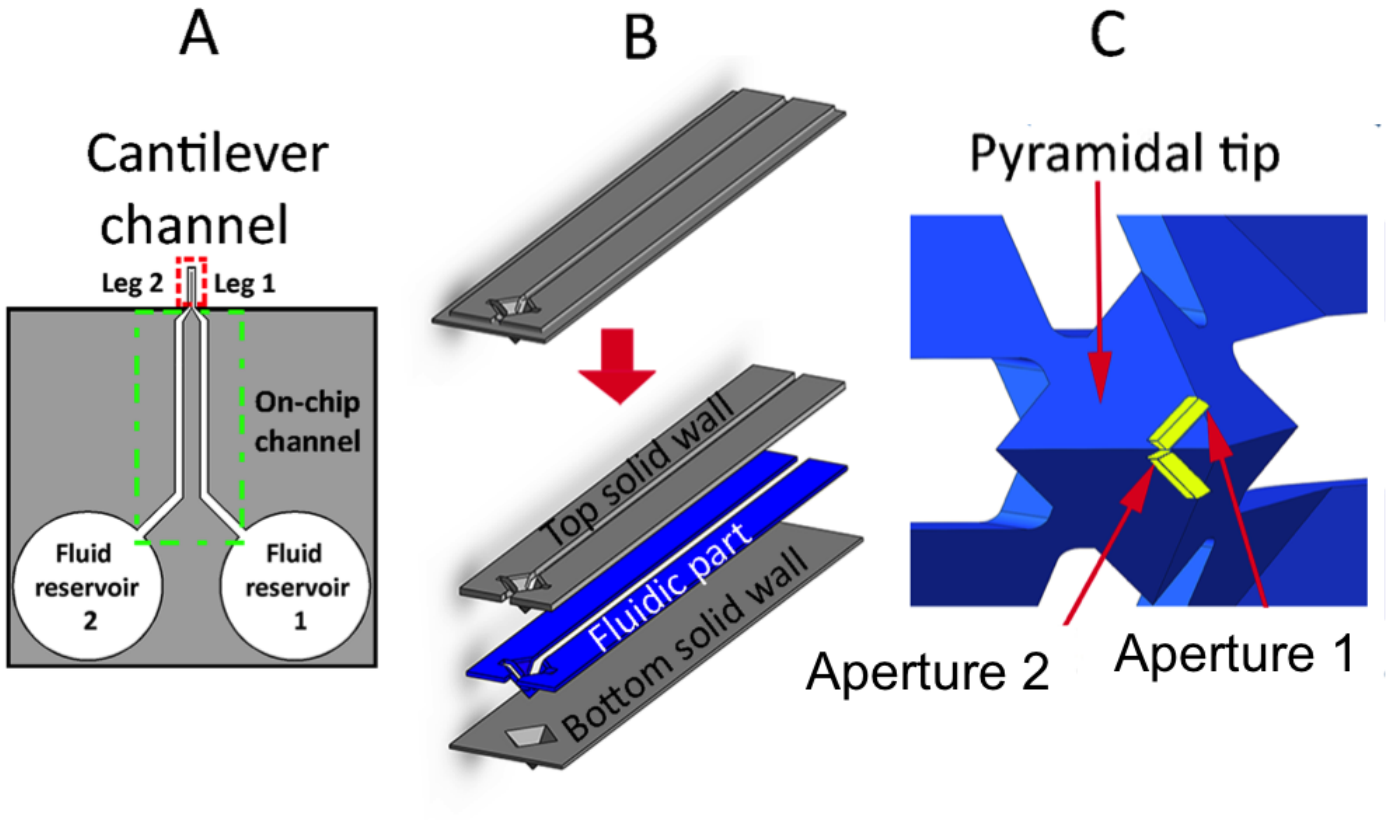

Figure S2: A) The schematic of the cantilever chip. The green-dashed box is on-chip channel and red-dashed box is the cantilever. For simulations, only red-dashed box is considered. B) Schematic view of the cantilever geometry that was used for FEM analysis. The exploded view of the design shows the top solid wall and the side-walls (grey), the fluidic part of the channel (blue) and the bottom solid wall (grey). C) Magnified view of the fluidic part at the cantilever tip; the pyramidal tip region where the channels merge and the fluidic outlets, the apertures, are indicated with red arrows.

Single Phase: As the first step, the simulations were validated by experimental results based on Table S2-case3. Figure S3 depicts the comparison of simulation and experimental data for single-phase fluids. In the experimental part (Figure S3A to S3C), first fluorescein was dispensed through Leg 1 (ΔP_Leg1=500 mbar and ΔP_Leg2=0 mbar) for 5s and after that outside water was immediately aspirated from Leg 2 (ΔP_Leg1=0 mbar and ΔP_Leg2=$-$50 mbar) for 5s. Figures S3A, S3B and S3C show 0 s, 0.5 s and 1 s (three consecutive frames) immediately after aspiration of outside water was started. As it can be seen in Figure S3B, after 0.5 s water starts filling Leg2 with a little decrease of fluorescein signal in this Leg. According to Figure S3C, after 1 s Leg 2 was almost filled with water as shown by arrows. After a trial and error procedure for different values of pressure drop between the pressure controller and cantilever legs, it was concluded that 60% pressure loss gives the best results in comparison with the experiments. Figures S3D, S3E and S3F depict 0 s, 0.5 s and 1 s after aspiration (ΔP*_Leg1=0 mbar and ΔP*_Leg2=$-$20 mbar) in the simulation in which only the cantilever is modelled without any external fluids (first approach). Note that "ΔP*" refers to the value of pressure at the cantilever legs, which means that all pressure losses between pressure controller and the point from which cantilever legs starts are considered on the value (mainly losses at the on-chip part of the channel). Figures S3G, S3H, and S3L are related to the similar mentioned times in the model with consideration of both inside the cantilever and surrounding outside fluid (second approach). As it can be seen, both approaches in the simulation, can predict the fluid behavior inside the cantilever. However, in the second approach, in which the surrounding fluid is considered, a smoother gradient of aspirated flow exist in concentration contour when t =5.5 s (compare Figures S3E and S3H). The reason is that in the first approach, it is assumed that the concentration of the aspirated flow

is always $0\,\mathrm{mol/m^3}$ (pure water without any fluorescein) but in the second approach, in the beginning of aspiration, some diluted fluorescein was aspirated into the cantilever again. After the transient (from dispensing to aspiration) behaviour both of them show similar concentrations. As it is shown in the figure, at 6 s and subsequent times, the concentration of fluorescein in Leg2 by the first and second approaches are obtained as $0.260\,\mathrm{mol/m^3}$ and $0.245\,\mathrm{mol/m^3}$ respectively which are fairly close to each other. Figure S3J shows the iso-concentration surfaces around the cantilever immediately when dispensing was finished and aspiration was going to be started. In this step, the concentration of fluorescein on the cantilever tip was $0.421\,\mathrm{mol/m^3}$ that was diluted in the outer region of the dispensed fluid. In the subsequent times (Figure S3K and S3L) the internal fluid was aspirated into the cantilever again but the outer region of the dispensed fluorescein was not changed a lot and was even slightly more diffused to the surrounding water. This behavior is quite similar to the experimental observations in Figure S3A to S3C. Figure S3M and N shows a quantified comparison between experiment and two different simulation approaches. In order to correlate the concentration and fluorescent intensity, a linear mapping was used. In this procedure, fluorescent intensity of 20 was mapped to $0.27\,\mathrm{mol/m^3}$ and fluorescent intensity of 52 was mapped to $0.421\,\mathrm{mol/m^3}$ and any values between these two values were mapped linearly.

Two Phase:The simulations were validated by experimental results based on Table S2-case5. Figure S4 depicts the comparison of simulation and experimental data for two-phase fluids. Figures S4N and S4P depict the experiment which was done for validation of two-phase simulation results (figures S4O and S4Q). In this experiment, as explained in Table S2-case 5, liquid phase (fluorescein) goes forward through leg1 of the cantilever in the way that we can see the meniscus between liquid (green) and air (black) which moves through this leg of the cantilever within 1 s. As it is seen in the simulation results, air (grey) and liquid (white) regions are quite the same. In cases that we cannot use fluorescent signals, this multiphase model can be used for any immiscible fluids to predict the meniscus position during time. See supplementary movie, simulation two phase.

3 Fluidic Interface

To enable fluidic connections, the hollow cantilever probe chip was glued to 3D printed (by stereolithography) fluidic interface. The fluidic interface has two reservoirs, each separately addressable through a side-channel (S5). The reservoirs of the cantilever chip were aligned to the reservoirs of the fluidic interface during the gluing process, by pushing the chip against the alignment blocks of the interface. In the side-channels of the fluidic interface, stainless steel tubes were glued. The stainless steel tube was connected to a flexible Tygon tubing for fluid flow.

4 Experimental setup

The experimental setup is shown in Figure S6. The description is given in the main text section 4.3.

5 Analytical model: Hydraulic Resistance

To gain insight into the flow behaviour of the 2-channel cantilever, an analytical model based on electrical circuit analogy was used. From Ohms law, $I = V/R$, where I is the current (analogous to flow rate Q), V is the voltage (analogous to applied pressure ΔP), and R is the resistance (flow resistance, $1/\alpha$). So for every applied pressure, fluid flows with a rate depending on the resistance offered by the micro/nanofluidic channels. In our situation, there are two pressure sources, two channels, a pyramid and two apertures where flow rate was analyzed. Furthermore, they are connected influencing each other and forming a fluidic network.

The pressure controller outlets (ΔP_{Leg1}, ΔP_{Leg2}) function as voltage sources, since they supply energy that instigates fluid flow in channels 1 and 2 and through the apertures (Q_{Leg1}, Q_{Leg2}, Q_A). The hydrodynamic resistance of the fluidic system was obtained by splitting the geometry into parts that could be approximated with a single hydrodynamic resistance formula (see S1). The resistances of the fluidic tubing and the fluidic interface were neglected, since the contributions were at least 2 orders lower compared to the fluidic resistances of the device. The complete hydrodynamic resistance model of the 2-channel cantilever chip is depicted in figure S7. This circuit was simplified to a model that contained 5 equivalent resistances, which is shown in S8. The resistances of the microfluidic channels were split up into two parts: the on-chip channel (Rchip.ch.) and the cantilever-part of the channel (Rcant. ch.), so that the pressure loss over the non-cantilever part could be calculated. Since a steady state, convection-only, single phase model was considered, no hydrodynamic capacitance, surface tension or diffusion was included in the network.

The hydrodynamic resistance model presented in figure S7 can give additional clarification for the experimental cases discussed. When dispensing with a 2-channel cantilever that has one reservoir filled with fluorescein (reservoir 1) and is immersed in water, the flow from reservoir 1 is distributed towards the other leg and out through the apertures. For case 2, when leg 1 is pressurized, but leg 2 is kept at atmospheric pressure, the equivalent resistance of the entire leg 2 was found to be Req_Leg2 = $6\,\mathrm{mbar-s/pl}$, while the equivalent resistance of the apertures was Req_A = $3.94\,\mathrm{mbar-s/pl}$. The analytical model predicts that Req_leg2/(Req_leg2+ Req_A (60%) of the flow will go through the apertures, while Req_A(Req_leg2+ Req_A) (40%) of the flow will go to the other channel, leg 2. The flow division ratio stays constant, even if the applied pressure on leg 1 varies (which results in different absolute flowrates). Besides cases where only one leg at a time is pressurized, the analytical model can also be used for cases where both

Table S1: Dimensions used to calculate the hydrodynamic resistances of the analytical model.

Part of the channel	Used formula	h ($\times 10^{-6}$ m)	L ($\times 10^{-6}$ m)	w ($\times 10^{-6}$ m)	w1 ($\times 10^{-6}$ m)	R (Pa.s/m^3)	R ($\times 10^{-2}$ mbar.s/pL)
on-chip channel, OC1	(2) tapered	1	58	9.5	25	3.87E+16	39
on-chip channel, OC2	(1) rectangular	1	586	25		2.57E+17	257
on-chip channel, OC3	(1) rectangular	1	182.50	30		6.64E+16	66
cantilever channel, CH	(1) rectangular	1	120.9	9.5		1.46E+17	146
cantilever channel, N1	(2) tapered	1	4.09	5.24	0.665	1.97E+16	20
cantilever channel, N2	(1) rectangular	1	0.5	0.665		1.53E+17	153
cantilever channel, E1	(1) rectangular	1	2.76	4.25		8.14E+15	8
cantilever channel, E2	(2) tapered	1	7.79	4.25	5.24	1.76E+16	18
pyramid, P	Sum of decreasing (3) squares	2.43=>0.265	1.51/500			3.23E+17	323
aperture 1, A1	(1) rectangular	0.3	0.4	0.97		2.03E+17	203
aperture 2, A2	(1) rectangular	0.37	0.4	1		1.10E+17	110

legs are pressurized. By solving the circuit of figure S7A through finding equivalent resistances and conducting mesh analysis, the following three formulas describing the flowrate, Q, (in pL/s) can be found below.

The equations derived are given in the main manuscript.

The applied pressure, ΔP, is entered in mbar. As the analytical model is based on the Hagen-Poiseuille equation, the flowrate is linearly depended on the applied pressures. A visual representation of the three flowrates for various pressure combinations on Leg 1 and 2 can be found in the main article. As Leg 1 and 2 are geometrically identical, the formulas given in the main article for leg resistances are still valid, except that the applied pressures are switched.

When applying the obtained relationships between the applied pressures and the resulting flowrates to Table S2-case 4, we can obtain the contribution to the flow through the aperture that comes from Leg 1 (filled with fluorescein). By changing the ratio Q_{Leg1}/Q_A we can tune the fluorescein concentration in the dispensed liquid. In figure 7 of the main article, it is visible that the water flows to leg 1 when the pressures $\Delta P_{Leg1} = 50\,\text{mbar}$ and $\Delta P_{Leg2} = 200\,\text{mbar}$ are applied. This experimental observation is confirmed by the flowrate analysis of Table S2-case 1. The flowrate in Leg 1 is negative, indicating a flow towards reservoir 1. All other flowrates of the three situations are positive, which also fits with the experimental observations. Table 4 of main article shows that by increasing the pressure on leg 1, while keeping the pressure on Leg 2 constant, the amount of fluorescein solution that is dispensed is increased. This is as expected and confirmed by the experimental results of Figure 7 of the main article. At t = 2s and 3 s, the size of the fluorescein droplet that leaves the hollow cantilever is the brightest and largest for case 3, for which also the highest Q_{Leg1}/Q_A is obtained from the hydrodynamic model.

6 Experimental conditions tested

All the experimental conditions tested are shown in the Table S2. We took several precautions to ensure reliability of the fluorescence data. 1) The auto intensity adjustment of the CCD was switched off during a particular measurement. 2) The exposure of the fluorophore was kept minimum to reduce any bleaching effect. 3) The devices were firmly fixed to avoid any motion of the chip. Movement of the device during measurements could blur the fluorescence intensity influencing the data. Considering all these precautions, the fluorescence data analyzed should be reliable.

7 Additional Dispensing data

The Figure S9 show the quantified values from single-phase numerical simulation (second approach with external fluid, Figure S3) for the mentioned Table S2-case 3, where in 5 s (from t = 0 s to 5 s) the fluorescein was dispensed and immediately after that, in 5 second (from t = 5 s to 10 s) the outside water was aspirated into the cantilever. The Figure S9 depicts the concentration (mol/m^3) and velocity distribution (m/s) of fluid during dispensing for three different ΔP*_Leg1 pressures of 100 mbar, 200 mbar and 300 mbar. The concentration profiles are shown during 5 s of dispensing of fluorescein when the cantilever is initially filled with water. The X-axis and Y-axis directions are shown in the schematic cantilevers above the figure. As shown in Figure S9A at 0 s, the concentration of fluorescein in the cantilever is 0 mol/m^3, and after 0.1 s, fluorescein concentration starts to go up. From 0.2 s to 5 s the cantilever is fully filled with the dispensed fluorescein. Since dispensed fluid enters from Leg 1 of the cantilever and X-axis is considered in the middle of leg 2, we do expect that a similar faster behavior of fluid exist in the Leg 1. As the applied pressure increases (Figure S9B and S9C), the flow rate increases and the cantilever will be filled with dispensed fluorescein much faster in the way that we cannot capture any concentration gradient along X-axis, and after 0.1 s the cantilever is completely filled with the dispensed fluid. The corresponding flowrates for these pressures in Leg1 are 29.8 pL/s, 59.6 pL/s and 88.3 pL/s and in Leg 2 are 19.0 pL/s, 38.0 pL/s

Table S2: Applied pressures on the corresponding fluid reservoir during the various experimental cases.

Case	Step No.	Step description	ΔP_{Leg1}(mbar)	ΔP_{Leg2}(mbar)	Time (s)
Back loading; Dispensing in àir	1.1	Fluorescein backloading	500	0	-
	1.2	Rhodamine-labelled liposomes backloading	0	1500	-
	1.3	Fluorescein dispensing	2000	0	-
	1.4	Rhodamine-labelled liposomes dispensing	0	2100	-
Back loading; Dispensing in water	2.1	Fluorescein backloading	500 (only done before the first condition tested)	0	-
	2.2	Fluorescein dispensing	10,20,30,40,50,100,200,500	0	30
Back and front loading; Aspiration in water	3.1	Fluorescein filling	500	0,0,0,0,0	5
	3.2	Water aspiration into leg 2	0	-10,-20,-30,-40,-50	20
Back and frong loading; Dispensing and aspiration in water	4.1	Fluorescein filling	500,500,500,500,500,500	0	5
	4.2	Water aspiration into leg 2	0,0,0,0,0,0	-50	20
	4.3	Dispensing of water	0,50,70,80,90,100	200	5
Back loading; Meniscus monitoring in air	5.1	Fluorescein back-loading	0	1700	
	5.2	Moving of fluorescein meniscus	0	200	0.665

and 56.4 pL/s respectively. In this condition, the correlation between flowrate, Q, (in pL/s) and pressure magnitude on cantilever legs, ΔP*, (in mbar) are extracted as equations Eq. 1 and Eq. 2 (with a fit of $R^2 = 1$) for Leg1 and Leg2 respectively.

$$Q_{Leg1} = 0.295 \times \Delta P^*_{Leg1}, \tag{1}$$

$$Q_{Leg2} = 0.188 \times \Delta P^*_{Leg1}, \tag{2}$$

The velocity distribution (m/s) of fluid inside the cantilever (at t = 4 s) is also shown by vector plots. The mentioned increases of flowrate at higher pressures are also clear from the velocity color bars in Figure S9A to S9C. Each vector is magnified using the magnification factor above each plot for a better visual presentation and fair comparison between different plots. The color of each vector shows the calculated velocity magnitude on the point from which each vector begins. As it is shown the maximum velocity occurs in the narrow region before the pyramidal tip.

8 Additional Aspiration data

8.1 Experimental data

Additional experimental data for ΔP_Leg1=0mbar and ΔP_Leg2=−50 mbar is shown in Figure S10. All fluorescent plots have been corrected by subtracting the background signal recorded at t = 0 s for every condition. Due to tilt in the chip, the entire channel from 0 µm to 670 µm was in the focal plane. The channel towards 670 µm was out of focus, leading to gradual decrease in the overall fluorescence intensity along the length. This was also corrected in both the experimental data for ΔP_Leg2=−10 mbar and −50 mbar shown in the main text and the supplementary respectively.

8.2 Simulation data

Additional simulation data for ΔP*_Leg1=0mbar and ΔP*_Leg2=-10mbar, -20mbar and -30mbar are shown in Figure S11.

9 Additional Transition Length data

Besides the zoomed-in version of the lower transition length values (Figure S12A), a full scale transition length map is shown in Figure S12B.

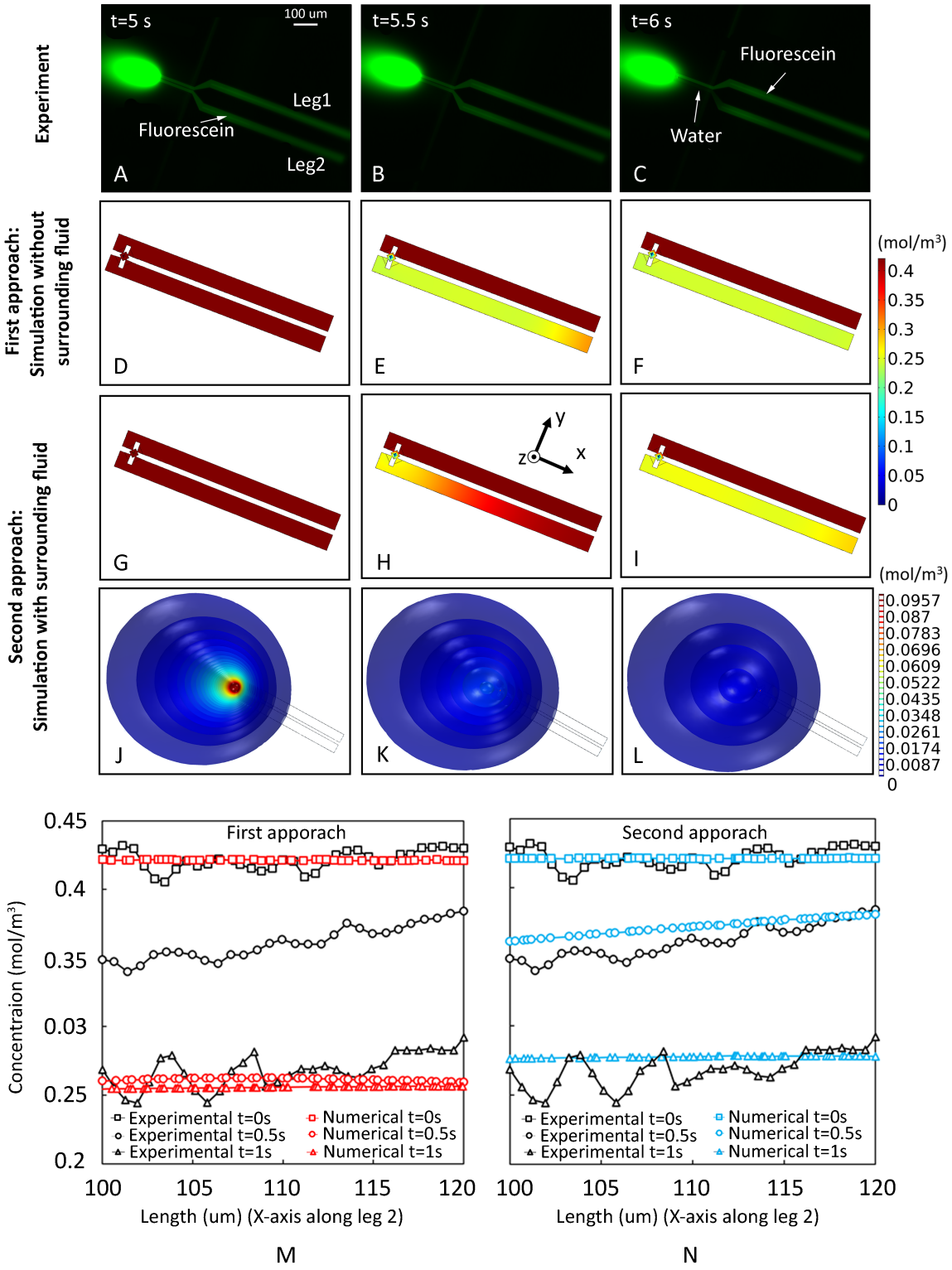

Figure S3: Comparison of fluorescence intensity from experimental tests and results obtained from simulations with and without external fluids around the aperture. (A) Experimental image at initial condition ($t = 5\,$s) (ΔP_Leg1=0 mbar and ΔP_Leg2=$-$50 mbar). (B) Eperimental image after $t = 0.5\,$s aspiration. (C) Experimental image after $t = 1\,$s aspiration. (D-F) Concentration contour (molmeter^3) obtained from FEM without considering surrounding fluid (ΔP*_Leg1=0 mbar and ΔP*_Leg2=$-$20 mbar) at the corresponding time frames ($0s, 0.5s$ and $1s$) to the experiments above them. (G-L) Concentration contour (mol/m^3) obtained from FEM by considering surrounding fluid (ΔP*_Leg1=0 mbar and ΔP*_Leg2=$-$20 mbar) at the corresponding time frames ($0s, 0.5s$ and $1s$) to the experiments above them. (M,N) Comparison between experimental and numerical concentration profiles along x-axis in the middle of leg2 from 100 µm to 120 µm for first and second approach respectively. P* is the pressure at the cantilever inlet, after the pressure loss due to on-chip channel from the applied pressure at the pressure controller.

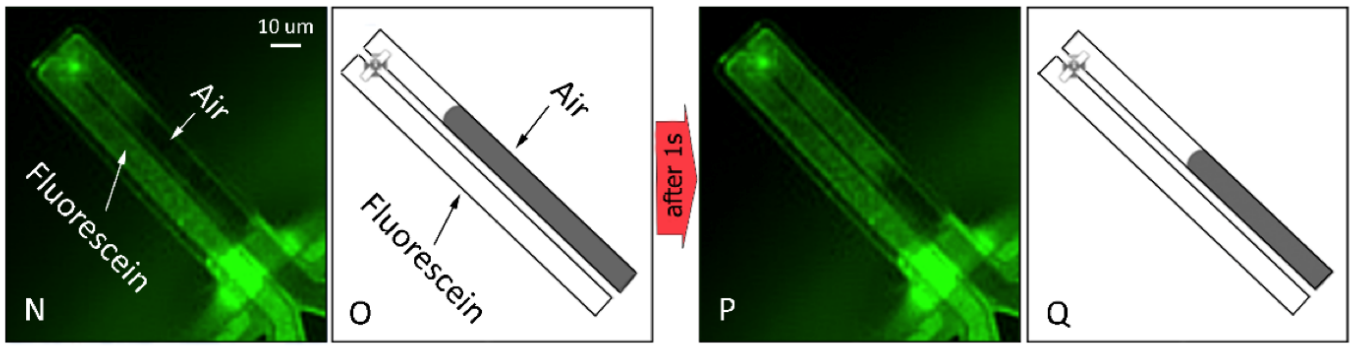

Figure S4: N) Fluorescence intensity from liquid-air experimental tests. O) Corresponding simulated situation, volume fraction of air (grey) and liquid (white) from FVM analysis. P) Experimental condition after 1 s. Q) Simulated condition after 1 s.

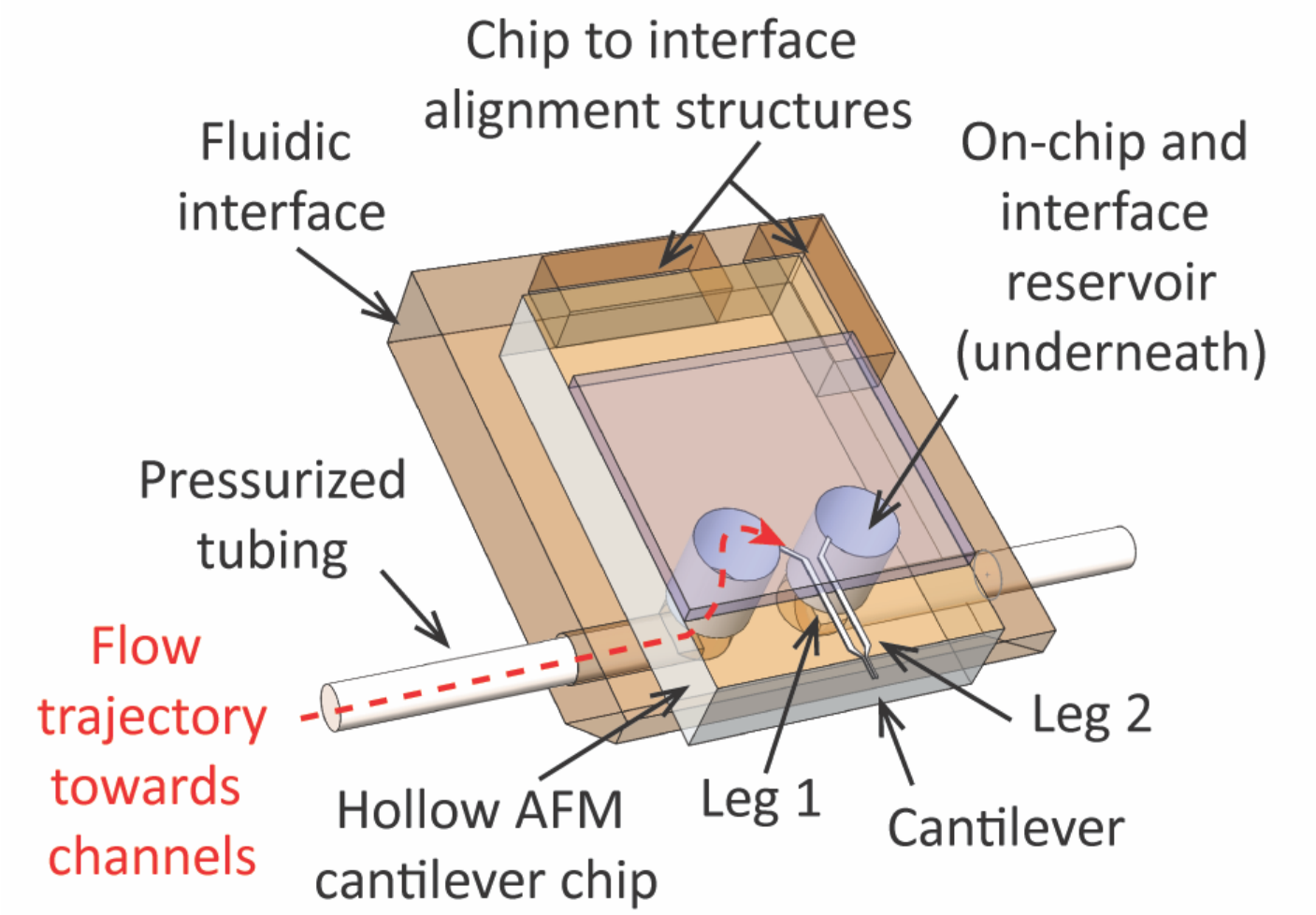

Figure S5: Schematic of the fluidic interface glued to the 2-channel cantilever chip (tip-side up). Two stainless steel tubes were glued on either side of the interface. The dashed line indicates the flow trajectory of the liquid from an external fluid reservoir towards the microfluidic channel.

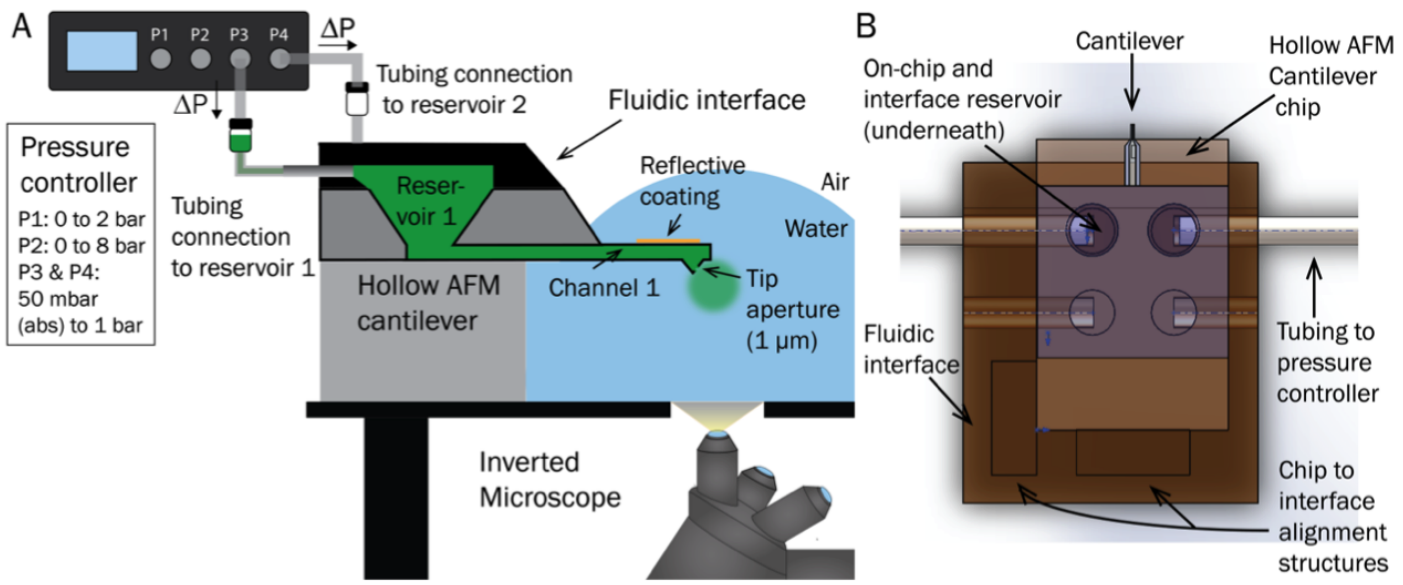

Figure S6: 1 A) Schematic of the experimental set-up used to image the multifluid manipulation with the 2-channel hollow AFM cantilever. B) CAD drawing of the fluidic interface that connects the hollow AFM cantilever with pressurized tubing.

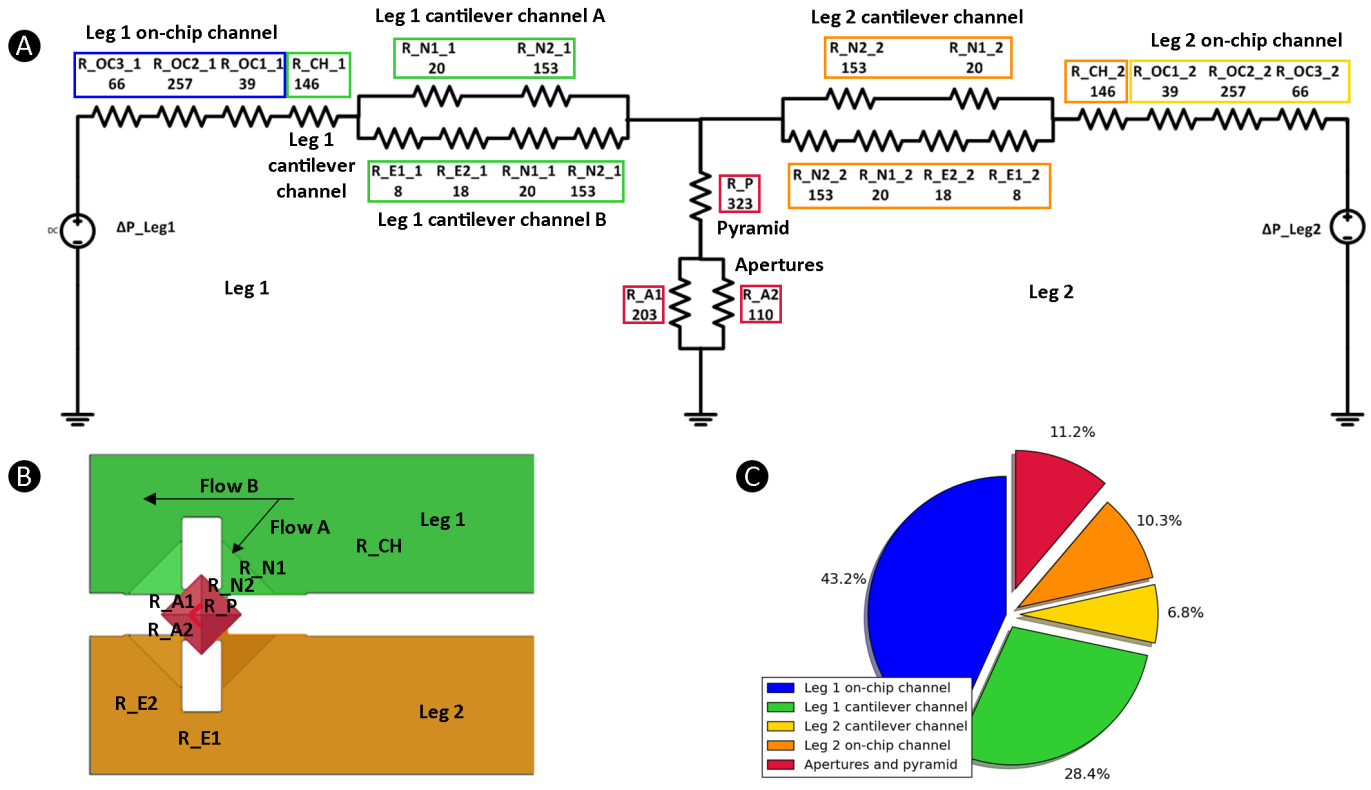

Figure S7: Hydraulic resistance of microfluidic network. A) Resistance of the individual fluidic element considered. B)Schematic of the various resistances as seen on the device. C) Pie chart of the contribution of resistances from various microfluidic elements.

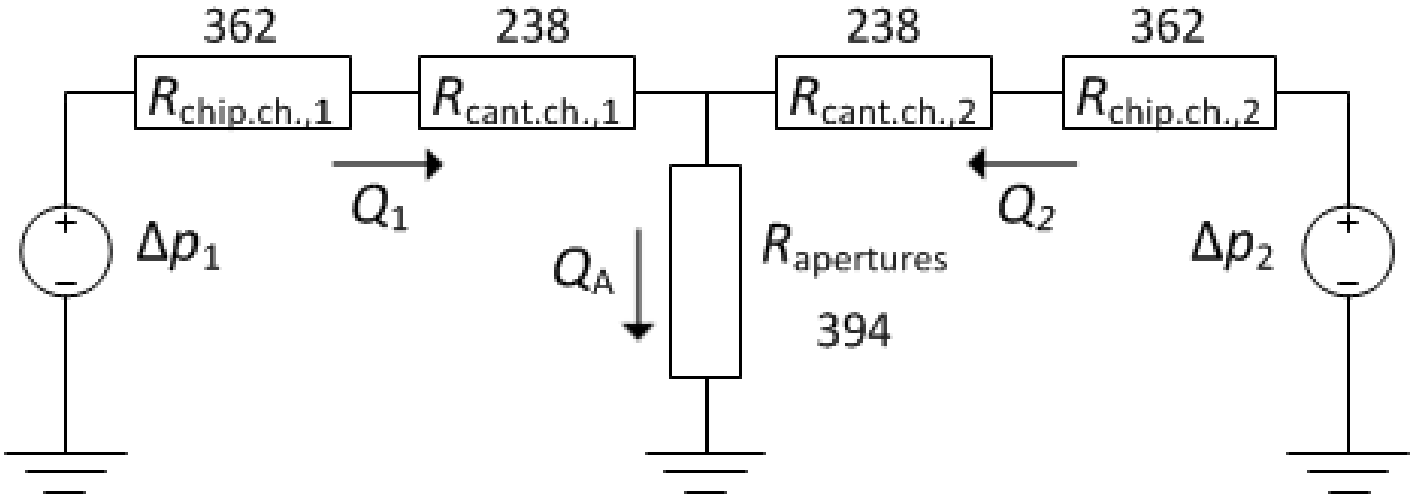

Figure S8: Equivalent hydrodynamic resistance model based on the geometry of a 2-channel cantilever. The various parts of the fluidic channels are depicted as resistances (R_x, values in 0.01 mbar $-$ s/pl)

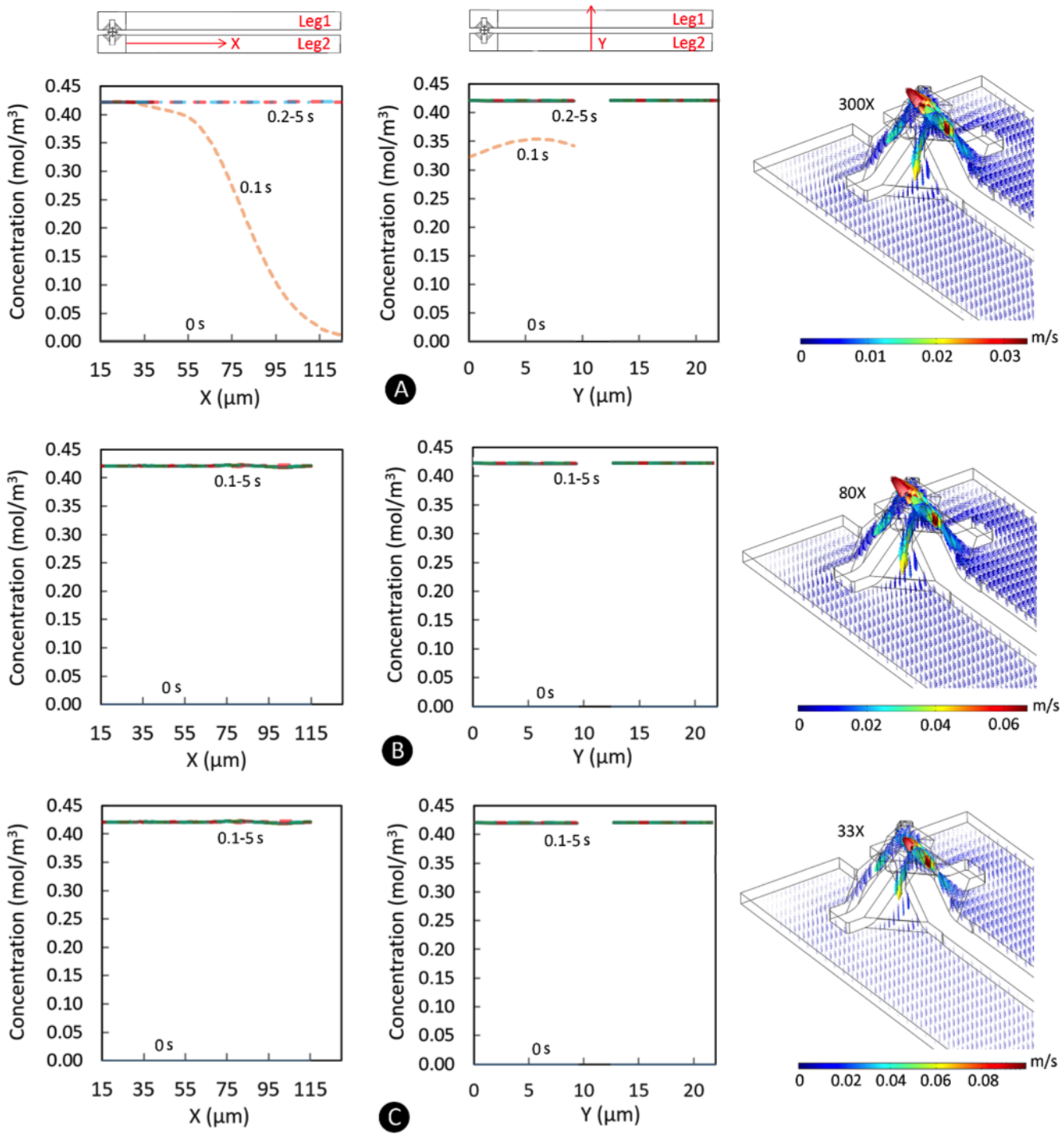

Figure S9: Concentration profiles (mol/m3) of fluorescein during 5 seconds dispensing along X and Y directions which are shown on the above schematic cantilevers. The cantilever is initially filled with water. The velocity distribution (m/s) of fluid inside the cantilever (at t=4s) is also shown by vector plots. Each vector is magnified using the magnification factor above each plot for a better visual presentation and fair comparison between different plots. The color of each vector shows the calculated velocity magnitude on the point from which each vector begins. As it is shown the maximum velocity occurs in the narrow region before the pyramidal tip (A) $\Delta P^*\_Leg1=100$ mbar, $\Delta P^*\_Leg2=0$ mbar (B) $\Delta P^*\_Leg1=200$ mbar, $\Delta P^*\_Leg2=0$ mbar (C) $\Delta P^*\_Leg1=300$ mbar, $\Delta P^*\_Leg2=0$ mbar. P^* is the pressure at the cantilever inlet, after the pressure loss due to on-chip channel from the applied pressure at the pressure controller.

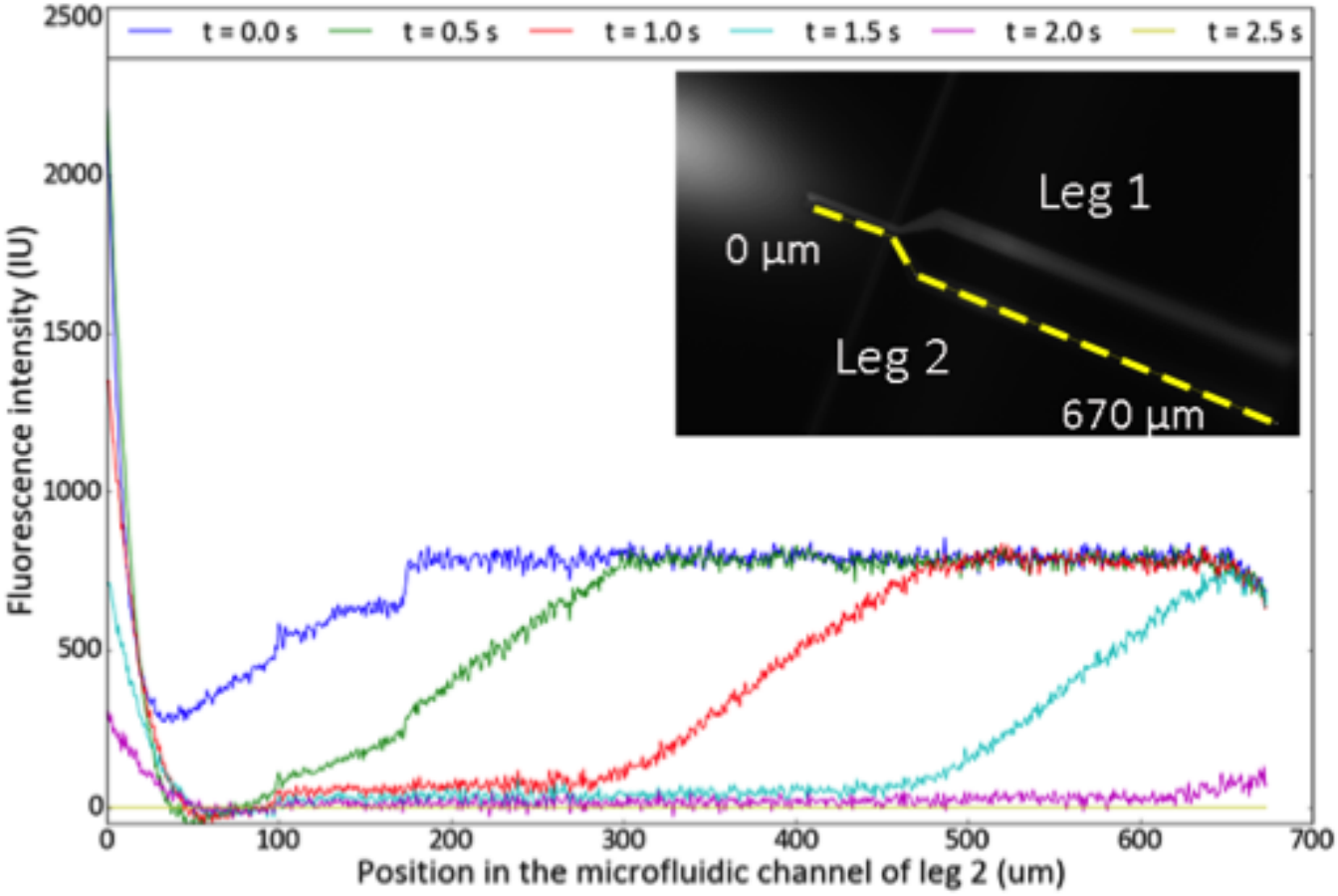

Figure S10: a) Fluorescent intensity profile of Leg 2 for ΔP_Leg1 = 0 mbar and ΔP_Leg2 = −50 mbar with time. The inset shows a snapshot taken during the ImageJ analysis of the intensity along the indicated dashed line; 0 µm is close to the cantilever tip, while 670 µm is in the on-chip part of the channel. Prior to water aspiration, the cantilever was filled with fluorescein solution, which created the 'droplet' near the tip area.

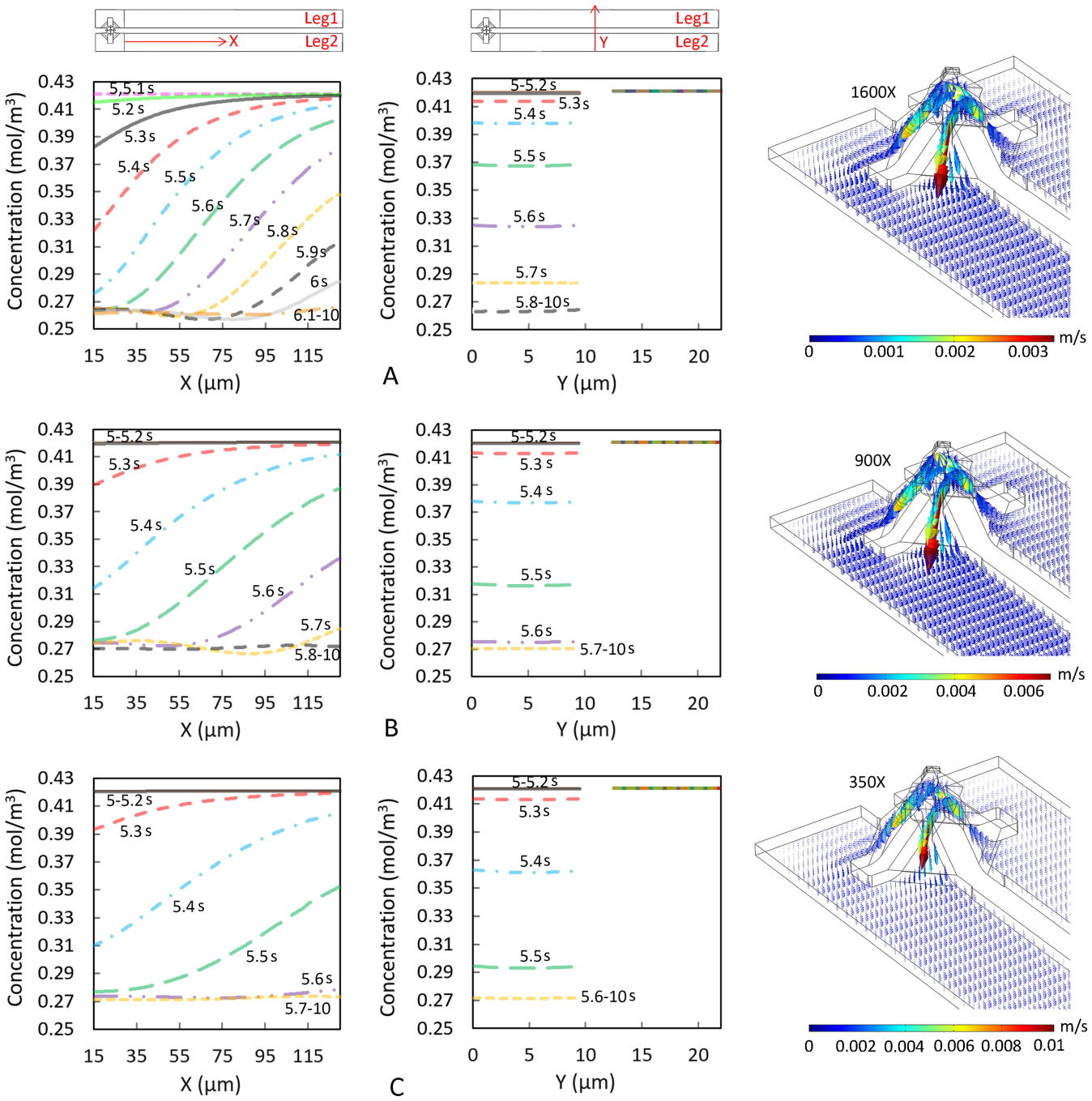

Figure S11: Concentration profiles (mol/m3) of fluorescein during 5 seconds aspiration when the cantilever is initially filled with fluorescein and then water starts going in from the aperture. X and Y directions are shown on the above schematic cantilevers. The velocity distribution (m/s) of fluid inside the cantilever (at t=9s) is also shown by vector plots. Each vector is magnified using the magnification factor above each plot for a better visual presentation and fair comparison between different plots. The color of each vector shows the calculated velocity magnitude on the point from which each vector begins. As it is shown the maximum velocity occurs in the narrow region before the pyramidal tip. (A) ΔP*_Leg1=0mbar, ΔP*_Leg2=-10mbar (B) ΔP*_Leg1=0mbar, ΔP*_Leg2=-20mbar (C) ΔP*_Leg1=0mbar, ΔP*_Leg2=-30mbar. P* is the pressure at the cantilever inlet, after the pressure loss due to on-chip channel from the applied pressure at the pressure controller.

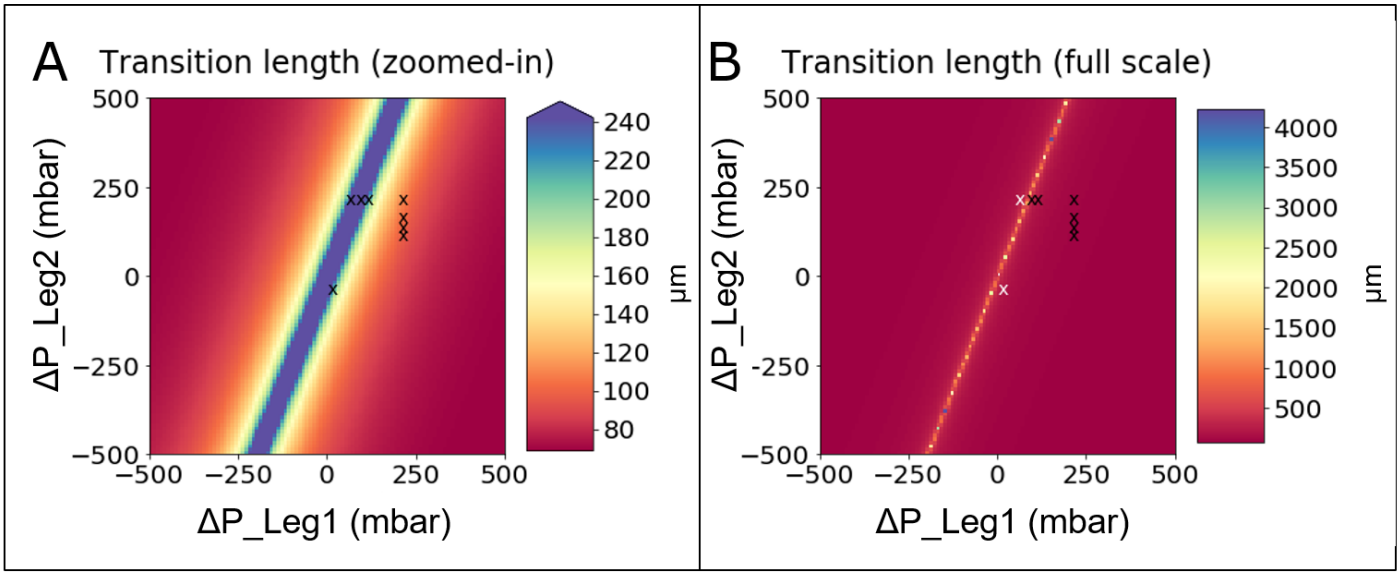

Figure S12: A-B Maps of the transition length for the entire pressure parameter space. A) A zoom-in of all transition lengths that have a value below 242 µm, a number that represents twice the cantilever channel length. All values above 242 µm are given the same colour blue. B) The full scale version of the transition length map.